

Wave-packet manipulation of He Rydberg states by a seeded free-electron laser

Mathieu Dumergue¹, Paolo Antonio Carpeggiani², Tamás Csizmadia¹, Miltcho Danailov³, Alexander Demidovich³, Giovanni De Ninno^{3,4}, Michele Di Fraia³, Per Eng-Johnsson⁵, Dominik Ertel⁶, Hikaru Fujise⁷, Mizuho Fushitani⁷, Luca Giannessi^{3,8}, Harshitha Nandiga Gopalakrishna¹, Akiyoshi Hishikawa^{7,9}, Heide Ibrahim¹⁰, Sergei Kühn¹, Francois Légaré¹⁰, Yu Luo¹¹, Praveen Kumar Maroju⁶, Johan Mauritsson⁵, Matteo Moiola⁶, Anna Olofsson⁵, Jasper Peschel⁵, Oksana Plekan³, Stephen T. Pratt¹², Lorenzo Raimondi³, Primož Rebernik Ribič³, Shu Saito¹¹, Giuseppe Sansone⁶, Ronak Shah⁶, Emma R. Simpson⁵, Daehyun You¹¹, Marco Zangrando^{3,13}, Carlo Callegari^{3,*}, Kiyoshi Ueda^{11,14,†} and Kevin C. Prince^{3,15,‡}

¹ELI ALPS, ELI-HU Non-Profit Ltd., Dugonics tér 13, H-6720 Szeged, Hungary

²Institut für Photonik, Technische Universität Wien, 1040 Vienna, Austria

³Elettra – Sincrotrone Trieste S.C.p.A., 34149 Basovizza, Trieste, Italy

⁴Laboratory of Quantum Optics, University of Nova Gorica, Nova Gorica 5001, Slovenia

⁵Lund University, Department of Physics, Lund, Sweden

⁶Physikalisches Institut, Albert-Ludwigs-Universität Freiburg, 79106 Freiburg, Germany

⁷Department of Chemistry, Nagoya University, Furo-cho, Chikusa, Nagoya, Aichi 464-8602, Japan

⁸INFN - Laboratori Nazionali di Frascati, 00044 Frascati, Rome, Italy

⁹Research Center for Materials Science, Nagoya University, Furo-cho, Chikusa, Nagoya, Aichi 464-8602, Japan

¹⁰INRS, Énergie, Matériaux et Télécommunications, 1650 Bld. Lionel Boulet, Varennes, Québec, Canada J3X 1S2

¹¹Institute of Multidisciplinary Research for Advanced Materials, Tohoku University, Sendai 980-8577, Japan

¹²Chemical Sciences and Engineering Division, Argonne National Laboratory, Lemont, Illinois 60439, USA

¹³CNR – IOM, 34149 Basovizza, Trieste, Italy

¹⁴Department of Chemistry, Tohoku University, Sendai 980-8578, Japan

¹⁵Department of Chemistry and Biotechnology, School of Science, Swinburne University of Technology, Melbourne 3122, Australia



(Received 6 March 2024; accepted 18 November 2024; published 27 December 2024)

We report a two-dimensional pump-control-probe spectroscopic study of the dynamics of singly excited He Rydberg-state wave packets with a seeded extreme ultraviolet (XUV) free-electron laser (FEL) source. A pair of coherent XUV pulses, defined by their coarse time separation and relative phase, created and manipulated the wave packets. The He atoms were postionized by infrared (IR) pulses, and the ion yield was measured as a function of XUV phase and IR arrival time. We tagged and sorted the relative phase of the XUV pulse pair on a single-shot basis by fitting each FEL spectrum with a suitable function that accounts for nonidealities of the XUV pulse pairs, associated with the seeding process; more generally, the fit returns the time-dependent electric field of the FEL spectra. The experimental two-dimensional maps of ion yields, measured as a function of IR (probe) delay and of XUV (pump-control) phase, were compared with the solution of the first-order time-dependent Schrödinger equation for this field. Despite the fact that the experimental conditions imply strong excitation, beyond the approximations of first-order perturbation theory, the simulated map satisfactorily reproduces the experimental one for temporally well-separated pulses. We show that by selecting data at appropriate values of pump-control phase, we enhance or suppress the amplitude of chosen wave-packet components consisting of two or more Rydberg states. When the temporal overlap of the pulse pair cannot be neglected, the phase reconstruction is underdetermined, and we provide a simplified comparison between data and simulations.

DOI: [10.1103/PhysRevResearch.6.043323](https://doi.org/10.1103/PhysRevResearch.6.043323)

I. INTRODUCTION

The electronic wave function of an atom excited to a superposition of resonant states by a coherent pulse of light exists as a wave packet that evolves over time. If the atom is irradiated by a second, delayed pulse of the same wavelength and well-defined relative phase, a second wave packet is excited, which interferes with the first [1–4]. Generally, this is manifested by an oscillation of populations as a function of time and gives rise to Ramsey fringes. The technique of measuring such phenomena is known as wave-packet interferometry and has been used for many years to obtain information about electronic and vibrational dynamics. Usually a signal whose

*Contact author: carlo.callegari@elettra.eu

†Contact author: kiyoshi.ueda@tohoku.ac.jp

‡Contact author: kevin.prince@elettra.eu

intensity is proportional to the population of excited states is measured, and since the probability of finding the system in the excited states is proportional to the modulus squared of the wave function, no phase information is available for the wave-packet dynamics. In a recent publication [5], it was shown that excitation by a single pulse, and ionization by a second pulse after a delay, can be used to extract very accurate values of the delay between the excitation and ionization pulses, but again, no wave-packet phase information was extracted. Ohmori *et al.* [6] showed that for double pulse excitation, and measurement of the signal $s(t)$ as a function of time t after the excitation, information about the wave-packet phase can be extracted, and we follow this approach in the present work.

While much work using double pulses has been done at laboratory laser wavelengths [7], there is less work available for short wavelengths, where the main light sources available are laboratory HHG sources and free-electron lasers (FELs). Koll *et al.* [8] summarized recent experimental progress using laboratory lasers, and they presented a study of hydrogen molecule ionization using a pair of phase-locked attosecond pulses. They highlighted the importance of the technique for investigating entanglement phenomena.

With FELs, production of coherent double pulses with attosecond phase control (as reflected in the observation of interference fringes in the FEL optical spectrum) was demonstrated at the seeded FEL FERMI [9]; the method relies on precise control of the relative phase of twin seed pulses, and it has been applied to studies of He, Ar, and HeNe dimers [10–12]. Timing jitter between the (inhomogeneous) electron beam and the seed introduces a shot-to-shot phase jitter, immediately apparent in the varying position of the fringes in the optical spectrum, and Uhl *et al.* [13] compensated for it by “realigning” the fringes in postanalysis. Wave-packet interferometry has been demonstrated at FLASH [14] and was applied to Auger electron interferometry and the study of ion dynamics in glycine [15,16]. Hikosaka and co-workers [17–19] claim to have performed coherent control with synchrotron radiation using a source with a bandwidth of 10% of the mean energy and crossed undulators. The model they used has been contested [20,21].

In this work, we describe a method to reconstruct precisely the electric field of each individual pulse pair, which in turn allows their use to study the temporal evolution of wave packets consisting of coherent superpositions of He Rydberg states. We describe analytically and take into account the properties of the pulse pair, in particular the shot-to-shot phase fluctuations, the effects of chirp, and the non-Gaussian temporal envelope shape of the excitation pulses. The envelope is described by a pair of Gaussian functions for weak seeding conditions and separated pulses, and it becomes a non-Gaussian pair with the onset of overbunching. This work represents a further contribution towards the development of FEL-based techniques for wave-packet interferometry, two-dimensional spectroscopy, and nonlinear optical studies.

II. EXPERIMENTAL METHODS AND SETUP

The experiments were performed at the Low Density Matter beamline [22] of the FERMI FEL. A Michelson-type interferometer was installed in the seeding optics of the FEL

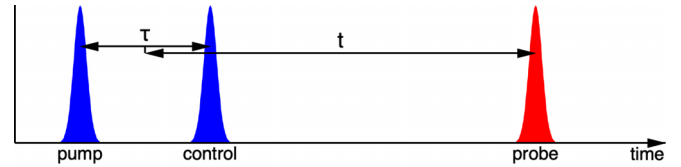


FIG. 1. Schematic illustration of the sequence of two FEL pulses, labeled pump and control, separated by a time τ and the ionizing IR pulse, labeled probe, arriving at time t . The midpoint between the two FEL pulses defines $t = 0$.

to split the seed pulse into two beams and delay one with respect to the other. The interferometer contained a pair of wedges for setting the fine delay, while a movable mirror set the coarse delay. The value of the delay was measured by blocking one of the arms and cross-correlating each pulse with an infrared (IR) pulse with the following parameters: wavelength 795 nm (1.560 eV), spot size 95 μm full width at half-maximum (FWHM), duration 55 fs. The IR pulse ionized the He atoms excited by the FEL pulses, and the ion yield was measured with a time-of-flight mass spectrometer. Wave packets were created by irradiating the He target with *double pulses* of sufficient bandwidth to excite a *manifold* of Rydberg states, and the He was as before ionized by the IR pulse. Figure 1 illustrates the pulse sequence.

Two pump-control delays were selected for this study, 390 fs (Dataset 1, well separated pulses) and 130 fs (Dataset 2, partially overlapping pulses). Nominal wavelengths of 50.62 nm (24.49 eV) for Dataset 1 and 50.59 nm (24.51 eV) for Dataset 2 were used, corresponding approximately to the band of Rydberg states from $n = 10$ to 16, i.e., within 150 meV of the first ionization potential of He. The chosen pump-control delays correspond to Kepler periods of wave packets consisting of two states with energy separations of 10.6 meV (390 fs) and 31.8 meV (130 fs), respectively. Our goal was to selectively excite or suppress various wave-packet components and investigate how the phase controls this process.

The spectrum of the radiation was measured shot-by-shot, and the full width at half-maximum bandwidth of the sum of all spectra in a set was about 40 meV. The pulse duration was measured by cross correlation and found to have a value of 100 fs. The two pulses were overlapped spatially, and the FEL pulse was focused to an elliptical spot of about 100 $\mu\text{m} \times 125 \mu\text{m}$ full width at half-maximum, while the IR pulse was focused to a circular spot of 100 μm full width at half-maximum. The total energy of the double pulses emitted by the FEL was typically 90 μJ for Dataset 1, and 60 μJ for Dataset 2. Assuming the calculated transmission of the beam-line optics, this implies energies at the experimental station of 18 and 11.5 μJ , respectively, and corresponds to average power densities of 1.89 and $1.26 \times 10^{12} \text{ W/cm}^2$.

Besides the electron-induced shot-to-shot phase-jitter mentioned above, a long-term drift arises from the fact that the interferometer used to generate the seed-pulse pair is not a common-path type, so there are unavoidable beam-path variations on the order of 1 or a few fs, due to mechanical drifts and temperature changes; this value is large compared to the radiation period of 168 as. Assuming a reasonable general

form of the electric fields of the pulses, based on an explicit modeling of the physics of generation of FEL pulses and a fit optimized for efficiency, we extracted the phase difference between the two pulses from the measured single-shot spectra of the radiation, as described below. Note that the phase difference here refers to the central frequency of the optical wave packet; different frequency components of the pulses have slightly different phases, as they complete different numbers of optical cycles during the delay.

Subsequent to the current experiment, a more stable and more sophisticated system was installed at FERMI [10,11,23], and the FERMI accelerator team was able to produce electron beams with lower chirp, i.e., the electron energy was more nearly constant along the electron pulse. That work was extended [13] to include the use of the optical spectrum recorded shot-by-shot to measure the phase relationship between the XUV pulses. The phase was determined from the position of the interference fringes in the spectrum: a central maximum corresponds to phase zero, and a central minimum to a phase difference of π .

In the present experiment, in addition to the drift of the relative phase, there was also longitudinal drift of the seed pulses along the electron bunch. In the accelerator configuration used, the electron energy was unavoidably slightly chirped, that is, it varied along the bunch, which implies that the wavelengths of the two pulses were slightly different. We show in this work a method to reconstruct precisely the electric field of each individual pulse pair; this allows the direct retrieval of the relative phase of the two pulses, and in addition the exploration of the effect of machine parameters on the properties of the FEL pulses under typical operating conditions that include a number of nonidealities. Furthermore, precise knowledge of the electric field of the pulses is crucial to describe exactly and study the temporal evolution of coherently excited wave packets, in this case He Rydberg states.

In addition, we performed temporal scans of the ionizing IR pulse, which was not done in the cited work [10,11], and which provides additional information about the wave-packet motion. The acquired ion signal was then plotted as a two-dimensional map of ion intensity versus phase and delay t . Oscillations of the signal as a function of phase at fixed t are due to the frequency components of the control pulse being in-phase with the pump pulse (increasing the population of a given Rydberg state) or in-antiphase (reducing the population), or at an intermediate value. Similarly, variations of the signal intensity as a function of t at fixed phase reflect the dynamics of the wave packet, as it moves radially: high intensity implies it is close to the nucleus, while low intensity occurs

when it is far from the nucleus. The information contained in the map can be analyzed and decomposed into the amplitudes and phase difference of the individual wave-packet components each consisting of two Rydberg states. We will show the validity of the approach, concentrating on one dataset (Dataset 1) acquired at a delay of 390 fs, then discuss its limitations in the case of partly overlapping seed pulses (Dataset 2, acquired at a delay of 130 fs).

For Dataset 1, the online spectrometer was calibrated immediately before data acquisition by scanning the FEL wavelength over the wavelengths of the $n = 7, 8,$ and 9 Rydberg states, with a fixed IR delay, and detecting the two-photon ionization signal. This calibrated the photon energies and spectrometer to the energies of the Rydberg states. The spectrometer calibration was then extrapolated to higher Rydberg states, and we estimated the error of this calibration to be <10 meV. For Dataset 2, the spectrometer was not calibrated immediately before the measurement, and the same calibration was assumed. The choice of scan parameters and delays was based on simulations performed prior to the experiment. The IR probe pulse delay was scanned in 25 (Dataset 1) and 37 (Dataset 2) time steps of 25 fs each.

Typically, the intensity map of the ion signal is analyzed with Fourier transforms [8]. However, this approach requires a large number of points over a wide control-probe delay interval in order to precisely identify the wave-packet components. Instead, for this experiment, we developed the procedure described in the next two sections.

III. MODELING OF PHOTON SPECTRA

With the FEL undulators tuned to produce harmonic $\eta = 5$ of the seed, we assume a twin seed pulse consisting of two Gaussian pulses separated by a fixed time τ and having an identical *intensity envelope* of width σ , central frequency ω_0 , and relative phase ϕ . With this choice of notation, $\sigma_F = \sigma/\sqrt{\eta}$, $\omega_F = \eta\omega_0$, $\phi_F = \eta\phi$ are the corresponding parameters for the twin FEL pulse; b_S, b_E are the dimensionless seed and electron-beam chirps. The twin pulse acts on an electron bunch of homogeneous density, and shot-to-shot fluctuations δt of the position of the twin pulse within the bunch cause a jitter of the FEL central frequency $\delta\omega_F = \alpha\delta t$, where α is the electron local linear chirp.

In the first part of the undulator of a high gain FEL amplifier, the field is directly proportional to the beam density modulation. Assuming that the field amplitude is well below the saturation level and following Gauthier *et al.* [24], the electric field of such a twin FEL pulse has the form

$$E(t) = E_0 J_\eta[\eta B|A(t)|] \exp[i\eta \arg A(t)] \exp\left[i\delta\omega_F t + 2ib_E \eta \left(\frac{t}{2\sigma}\right)^2\right], \quad (1)$$

$$A(t) = \exp\left[-(1 - 2ib_S)\left(\frac{t - \tau/2}{2\sigma}\right)^2 + i\omega_0(t - \tau/2) - i\phi/2\right] + \exp\left[-(1 - 2ib_S)\left(\frac{t + \tau/2}{2\sigma}\right)^2 + i\omega_0(t + \tau/2) + i\phi/2\right], \quad (2)$$

where $A(t)$ is the field of the twin seed pulses, J_η is the Bessel function of the first kind of order η , and B is proportional to the dispersive strength of the magnetic chicane that is part of the seed scheme.

In the weak-field limit, $J_\eta(x)$ behaves like $\frac{x^\eta}{2^\eta \eta!}$, so that when $\eta B|A(t)| \ll 1$, within a proportionality constant Eq. (1) becomes

$$E(t) \propto [A(t)]^\eta \exp \left[i\delta\omega_F t + 2ib_E \eta \left(\frac{t}{2\sigma} \right)^2 \right], \quad (3)$$

which, if the overlap of the two Gaussian pulses can be neglected, reduces to

$$E(t) \propto \left\{ \exp \left[-\eta \left(\frac{t - \tau/2}{2\sigma} \right)^2 \right] \exp(-i\eta\omega_0\tau/2) \exp \left[2ib_S \eta \left(\frac{t - \tau/2}{2\sigma} \right)^2 \right] \exp(-i\eta\phi/2) \right. \\ \left. + \exp \left[-\eta \left(\frac{t + \tau/2}{2\sigma} \right)^2 \right] \exp(+i\eta\omega_0\tau/2) \exp \left[2ib_S \eta \left(\frac{t + \tau/2}{2\sigma} \right)^2 \right] \exp(i\eta\phi/2) \right\} \exp(i\omega_F t) \exp \left[i\delta\omega_F t + 2ib_E \eta \left(\frac{t}{2\sigma} \right)^2 \right]. \quad (4)$$

Equation (4) has an analytical Fourier transform:

$$\hat{E}(\omega) \propto \exp \left\{ -\frac{[\sigma_F(\omega + \omega_F + \delta\omega_F) + b_E\tau/(2\sigma_F)]^2}{1 - 2i(b_E + b_S)} + i\frac{(\omega + \delta\omega_F)\tau}{2} - i\eta\phi/2 \right\} \\ + \exp \left\{ -\frac{[\sigma_F(\omega + \omega_F + \delta\omega_F) - b_E\tau/(2\sigma_F)]^2}{1 - 2i(b_E + b_S)} - i\frac{(\omega + \delta\omega_F)\tau}{2} + i\eta\phi/2 \right\}. \quad (5)$$

It is interesting to look at the expression for $|\hat{E}(\omega)|^2$ in the limit of Eq. (5):

$$|\hat{E}(\omega)|^2 \propto \exp(p)[2\cos(r) + 2\cosh(s)] \quad (6)$$

with

$$p = -\frac{4\sigma_F^2(\omega + \omega_F + \delta\omega_F)^2 + (b_E\tau/\sigma_F)^2}{2[1 + 4(b_E + b_S)^2]}, \quad (7)$$

$$r = (\omega + \delta\omega_F)\tau - \eta\phi - \frac{4b_E(b_E + b_S)}{1 + 4(b_E + b_S)^2}(\omega + \omega_F + \delta\omega_F)\tau, \quad (8)$$

$$s = \frac{2(\omega + \omega_F + \delta\omega_F)b_E\tau}{1 + 4(b_E + b_S)^2}, \quad (9)$$

where Eqs. (6) and (8) show the phase dependence of the FEL spectrum, as well as the deviation due to the chirp from the ideal case: $[\cos(\omega\tau - \eta\phi) + 1]$. In the general case, Eq. (1) does not have an analytical Fourier transform; furthermore, we wish to include the instrumental broadening of the spectrometer.

IV. FITTING OF PHOTON SPECTRA

The above equations were implemented for Dataset 1 in a numerical approach (based on a Python script) where Eq. (1) is used to generate a set of values whose fast Fourier transform returns the values of $\hat{E}(\omega)$ at the points measured by the photon spectrometer. From these, $|\hat{E}(\omega)|^2$ is calculated and convoluted with a Gaussian of fixed width $\sigma_s = 1.86736$ pixel [2.18 meV; 1 pixel ≈ 1.17 meV; the value of σ_s was sampled from 1.65 to 2 pixels in steps of 0.05 pixel, and then the (interpolated) value was chosen that minimized the χ_r^2 distribution]. The resulting array is fed to a least-squares minimization function producing the results, of which a sample is shown in Fig. 2. This example illustrates how an acceptable fit can be obtained by ignoring chirp and dispersion (B), but the fit is poorest in the wings of the spectrum. By including

both effects, a far better fit is obtained in the wings, where it was occasionally observed that the fringe spacing deviated from the average value. The approach is sufficiently fast that the whole Dataset 1 of 37 500 individual shots (25 000 signal shots and 12 500 blank shots for background subtraction) can be processed in less than an hour. A subset of the spectra was visually inspected to ensure that the fitting protocol was well-behaved. Each of the best-fit parameters was then histogrammed, and the results are shown in Fig. 3; in all cases, the distribution is narrow and physically meaningful, that is, the values are similar to those expected or measured in the past. It is worth noting that ignoring the role of dispersion (B), i.e., using Eq. (4) for the fit, returns a fit of lesser quality but still visually acceptable, with the main difference being the larger, and more scattered, values found for the chirp parameters; see Fig. 9 in the Appendix.

The parameter τ accounts for both the pulse separation (determining fringe spacing) and phase (determining the fringe position) and the former is sufficiently stable (few fs drift), so it can be fixed for all the shots to the value set in the experiment: -390 fs. We introduce a phase $\phi_F \in [0, 2\pi]$ as a variable fit parameter. σ_F , b_E , b_S , $\delta\omega_F$, B were allowed to vary; ω_F was set *a posteriori* to the value that makes the ensemble average $\langle \delta\omega_F \rangle = 0$. As explained below, the fit parameter ϕ_F is then corrected by an amount $\delta\omega_F\tau$ prior to binning. Using a Python script on a dedicated server, the total time to fit every spectrum in a file of 100 single-shot FEL spectra with the numeric approach just described was a few seconds, indicating our method is computationally economical. The data were filtered to reject empty shots, very low pulse energies, and unrealistic signals; the rejected shots amounted to a few percent of the total. The envelope and phase (minus the linear part) of the electric field [Eq. (1)] are shown in Fig. 4 for the case $\phi_F = 0$, with the amplitude E_0 calculated from the experimental parameters, and approximating the spatial distribution by a flat-top profile. This result corresponds to the best-fit parameters, except for b_E , b_S , for which the values

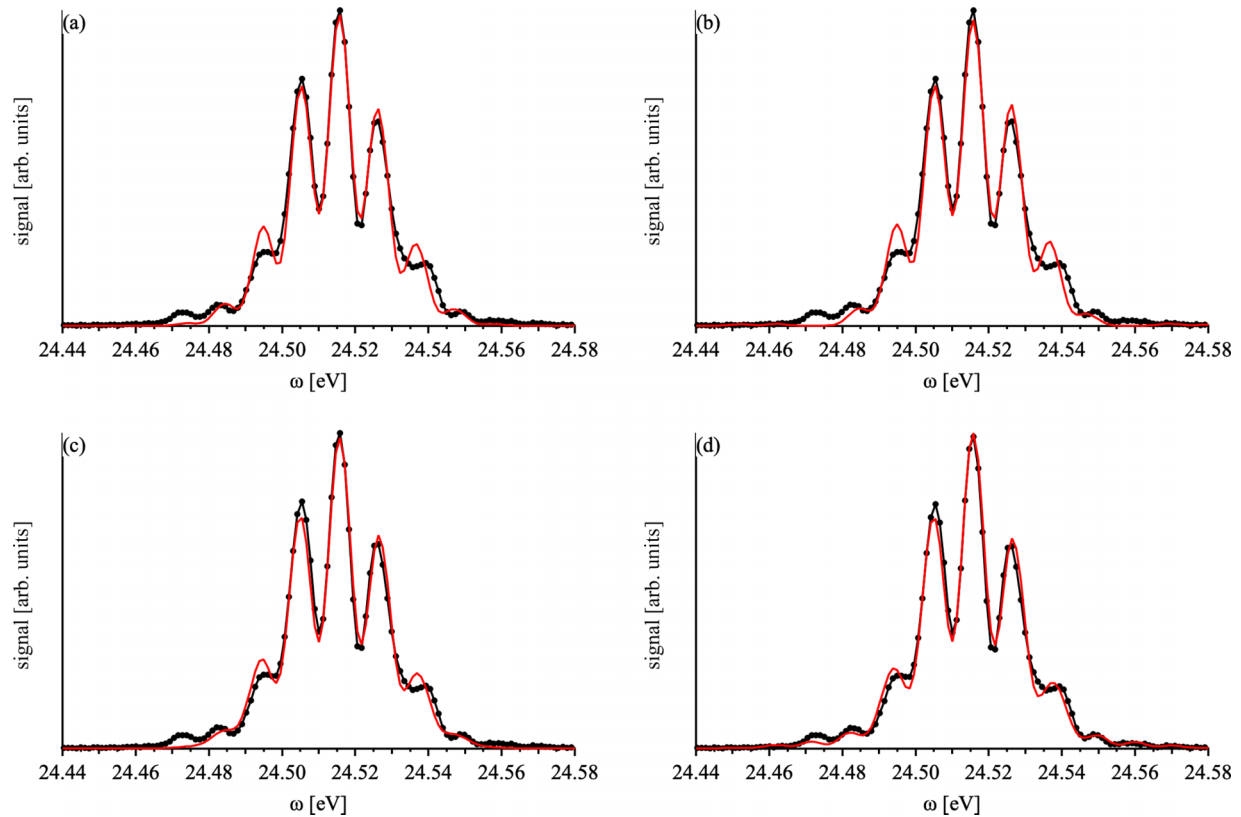


FIG. 2. Best fits of a single-shot FEL spectrum. (a) Chirm and dispersion B ignored; (b) chirm ignored, B included; (c) chirm included, B ignored; (d) chirm and B included. The fitted phase values are -0.487 , -0.440 , -0.389 , and -0.414 , respectively.

at the maximum of the joint histogram were chosen. This information will be used to simulate the ion maps (with t and ϕ_F as independent variables) as described in the next section. The parameters used are reported in Table I. Note that the pulses are non-Gaussian, with a small local minimum at the center. This is a consequence of the high dispersion (B) used to generate the pulses, and consequent onset of overbunching [11,24].

For Dataset 2, the same numerical approach was used, but as will become clear below, the situation is less straightforward when the pulses partially overlap.

V. RESULTS AND ANALYSIS OF PHOTOION SIGNAL: 2D MAPS

A. Generation

Information from Sec. IV was used to sort the single-shot signal (He^+ peak integral) into 20 phase bins, each 0.1π wide. In addition, the single-shot FEL energy (integral of the photon pulse) was separately accumulated for each phase bin and used to normalize the accumulated ion signal. The procedure was repeated for each IR delay, returning a two-dimensional (2D) map of signal as a function of IR delay and phase ϕ_F . Note that prior to binning, the fit parameter ϕ_F was corrected by an amount $\delta\omega_F\tau$: inspection of Eq. (1) shows that upon Fourier transform, $\delta\omega_F$ results in a rigid shift of the position of the fringes. Because $\delta\omega_F$ accounts for jitter of the center frequency induced by the electrons, the fact that the aforementioned correction results in much better contrast of the 2D

delay-phase map (Fig. 5) suggests that phase stability of the seed alone is not sufficient in this kind of experiment.

B. Modeling

With the functional form of the electric field described in Sec. III, we simulated the 2D maps of the signal versus FEL-IR delay and the relative phase of the twin pulses. For reasons that will become clear below, our modeling was performed using arbitrary, rather than absolute, units, and the results were normalized to a maximum of unity. Our method is based on first-order perturbation theory and assumes the rotating-wave approximation. We follow the approach of Noordam *et al.* [4], whose notation is slightly different, in particular $\omega_F \leftrightarrow \omega_L$ and $\tau \leftrightarrow \tau_d$. Equation (2) therein for the probability amplitude of exciting into the state $|np\rangle$ reads

$$a_n(t) = -ie^{-i\omega_n t} \frac{\mu}{n^{3/2}} \int_{-\infty}^t dt' E(t') e^{-i\omega_{1n} t'}. \quad (10)$$

ω_n is the energy of state n , $\omega_{1n} = \omega_n - \omega_1$ is the $|1s\rangle \rightarrow |np\rangle$ transition energy, and μ is a scaled dipole matrix element. For a Gaussian pulse

$$E(t; t_0, \phi_F, \sigma_F) = \frac{e^{-\left(\frac{t-t_0}{2\sigma_F}\right)^2 - i\phi - i\omega_F(t-t_0)}}{\sigma_F \sqrt{\pi}}, \quad (11)$$

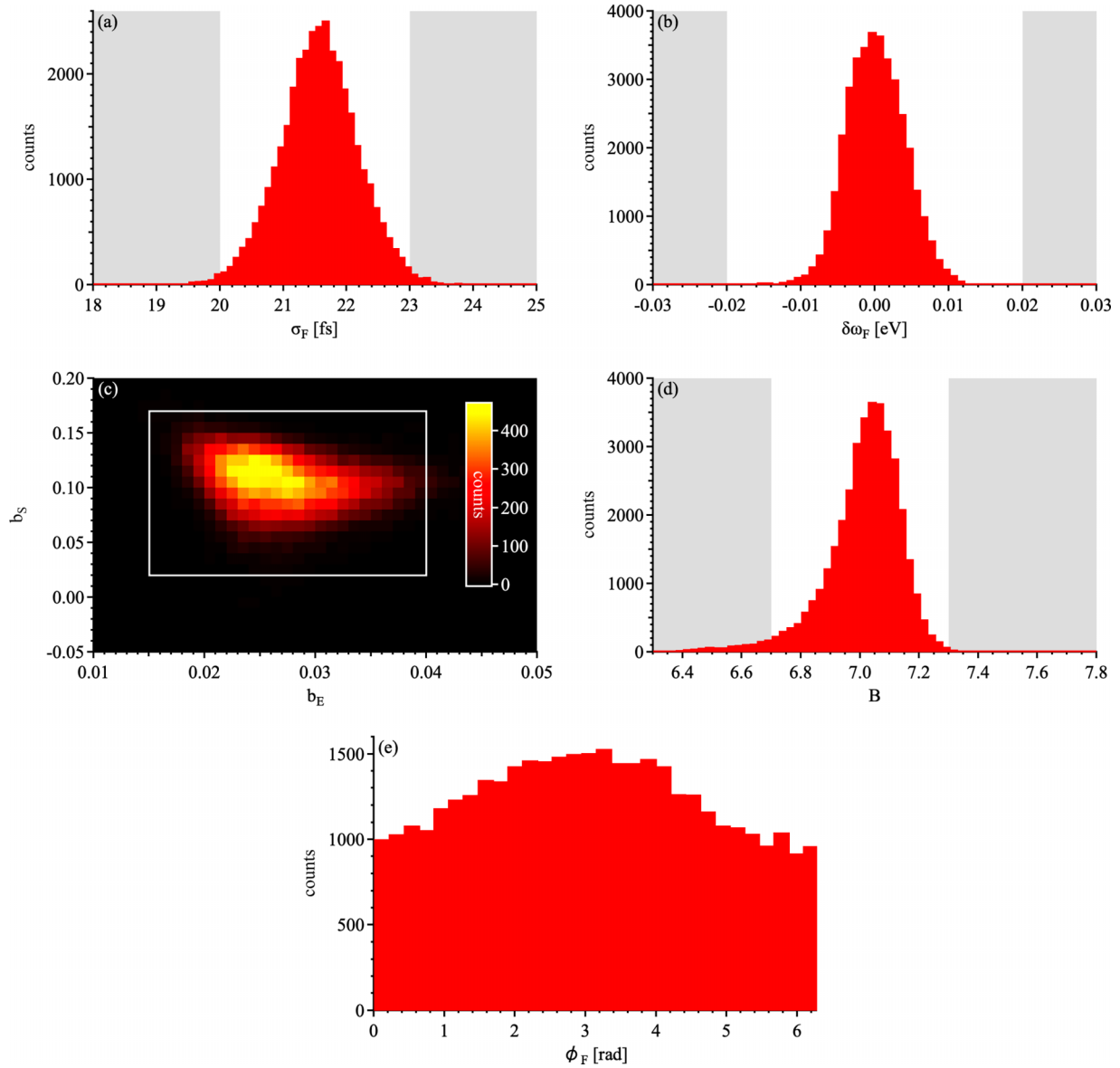


FIG. 3. Best-fit parameter histograms. (a) σ_F , (b) $\delta\omega_F$, (c) b_E , b_S , (d) B , and (e) ϕ_F . The shaded areas [the white box for panel (c)] indicate the limits chosen for rejection of outliers in the generation of 2D maps; see Fig. 5.

the integral reads

$$e^{-(\Delta\omega_n\sigma_F)^2} \operatorname{erfc}\left(-\frac{t-t_0}{2\sigma_F} - i\Delta\omega_n\sigma_F\right) e^{-i\omega_{1n}t_0 - i\phi_F}, \quad (12)$$

where $\Delta\omega_n = \omega_F + \omega_{1n}$ is the detuning from level n . Note that for large enough IR delays, when the effect of the FEL pulses is essentially complete, we can replace the upper integration

limit in Eq. (10) with ∞ , thus

$$\begin{aligned} a_n(t) &\approx -ie^{-i\omega_{1n}t} \frac{\mu}{n^{3/2}} \int_{-\infty}^{\infty} dt' E(t') e^{-i\omega_{1n}t'} \\ &= -ie^{-i\omega_{1n}t} \frac{\mu}{n^{3/2}} \hat{E}(-\omega_{1n}), \end{aligned} \quad (13)$$

where $\hat{E}(-\omega_{1n})$ is the Fourier component at resonant frequency $-\omega_{1n}$.

TABLE I. Best-fit parameters of the FEL photon spectra (average over all single shots of Dataset 1; standard deviation in parentheses). For b_E and b_S , the most probable values of the joint histogram are also given in the second row. Boldface values are fixed. See the text for details.

σ_F (fs)	b_E	b_S	ω_F (eV)	B	τ (fs)
21.55 (0.58)	0.027 (0.005)	0.105 (0.023)	24.5128	7.02 (0.11)	390
	0.0245	0.115			

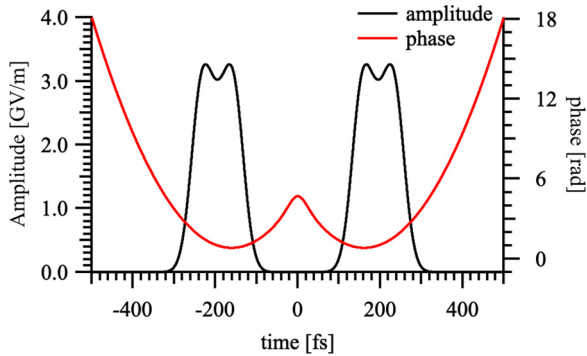


FIG. 4. Amplitude and phase (minus linear part) of the complex electric field obtained from Eq. (1) with the best-fit parameters reported in Table I (for b_E and b_S , the most probable values of the joint histogram are used; see the text), and $\phi = 0$.

The analytical treatment above is interesting as it yields an impression of the expected signal. The general case that we wish to reproduce, based on Eq. (1), requires Eq. (10) to be integrated numerically; we wish to calculate the observed signal $s(t)$,

$$s(t) \propto \left| \sum_n w_n a_n \right|^2 = \sum_k w_k^2 |a_k|^2 + \sum_{k>m} w_k w_m (a_k a_m^* + a_k^* a_m), \quad (14)$$

where w_n are real-valued weights accounting for the ionization probability of state n ; we assume $w_n = 1/n^{3/2}$ [25,26]. Let us note that in the limit of large t , irrespective of the exact form of $E(t)$, the quantities $|a_n|$ and $|a_n a_m^*|$ do not depend on t [Eq. (13)], and we will plot them for Dataset 1 (Fig. 7) to show the population of each state n , and the contribution of each “wave-packet component” (n, m).

To provide an intuitive model, we discuss in the Appendix the case of two δ -like pulses, which is valid in the approximation that the signal maps are deconvoluted of the instrument response function (assumed to be Gaussian). In this approximation, the equations simplify and the map can be considered as a sum of constants (for $k = m$) plus cosine functions whose frequencies are those of the Rydberg wave-packet components; their amplitude depends on the delay τ and the phase ϕ_F .

C. Simulation

Numerical integration of Eq. (10) with the best-fit parameters reported in Sec. IV returns coefficients $a_n(t)$ that we use as input to Eq. (14). Doing this for each of the phase and IR delay values of the experimental 2D map returns the simulation in Fig. 6(a). Upon varying the central wavelength from the nominal value, it was found that this map is very sensitive to the exact value of ω_F , and the frequency offset was more than the estimated uncertainty in the calibration of the spectrometer. This is to be expected: the calibration was not performed at the wavelengths used, but at nearby wavelengths and then extrapolated, whereas the spacing of the He states is (by design of the experiment) a fraction of the linewidth. Furthermore, we can expect that the ultimate sensitivity of the simulation is a fraction of a fringe, thus well below a tenth of

the linewidth. We generated several maps in regular steps of ω_F and chose the one most similar to the experimental map, based on visual inspection, Fig. 6(b). Note that the features of the simulated maps are sharper than those of the experimental map (Fig. 5, right), because they do not consider the finite duration of the IR pulse. The spectrometer offset of 21 meV is significantly larger than our estimated error of 10 meV.

D. Rydberg state populations and wave-packet contributions

To estimate the absolute Rydberg populations, the electric field calculated above was inserted into Eq. (10), and a_n was calculated by numerically integrating this equation. For the strongest Rydberg state, $n = 12$, we found a maximum value of $|a_n|^2 = 1.2$ for values of phase = 0.6 rad, which is obviously unphysical, and the assumption of perturbation theory that $|a_n|^2 \ll 1$ is clearly not fulfilled. To perform a more accurate calculation, it would be necessary to solve numerically the set of coupled differential equations describing the probability amplitudes of all states, as was done in Ref. [27]. However, this is beyond the scope of the present work. Nevertheless, as we have seen, the theory and calculations provide a good description of the experimental results. This is surprising, and there are several reasons why this might happen. Experimentally, any small misalignment of the transport optics diminishes the pulse energy, so it may have been lower than the estimated value. In addition, volume averaging effects in the real spot profile imply that there are significant contributions from low irradiance volumes. Finally, it is also possible that perturbation theory yields a sufficiently accurate result even when the basic assumptions are not fulfilled.

As mentioned above, for large values of the ionizing IR pulse delay t , such that the effect of the twin FEL pulses is completed, the amplitude $|a_n|$ of each quantum state n in the wave packet, as well as the contribution $|a_n a_m^*|$ of each wave-packet beating component (n, m), do not change with t . We take their values at the largest t in our numerical solution, 900 fs, and plot them in Fig. 7.

Figure 7 shows, as a function of optical phase, (a) the calculated amplitude of each Rydberg state; (b) the contribution to the ion signal of each wave packet; and (c) the extracted wave-packet phase. As stated above, the phase refers to the central wavelength of the light pulses. If the phase accumulated during the delay between the two light pulses is zero for this wavelength, then it is nonzero for other wavelengths within the bandwidth of the pulse, since they have a longer or shorter period. 390 fs corresponds to approximately 2310 cycles. If the central wavelength is 50.6227 nm, for example, and the delay is 390 fs, the phase may be zero. At a wavelength of 50.6204 nm (He $1s12p$ Rydberg) and for the same delay of 390 fs, the phase is 0.34 rad with respect to the central wavelength. The difference in wavelength corresponds to a difference of 1 meV in photon energy.

Bearing this in mind, we can interpret the results in Fig. 7. The $n = 12$ Rydberg state displays a maximum near 2π , at about 5.7 rad; it does not occur at 2π because the excitation wavelength is slightly displaced from the central wavelength of the pulse. At 2.6 rad, there is strong destructive interference, and the amplitude of this Rydberg state goes to zero.

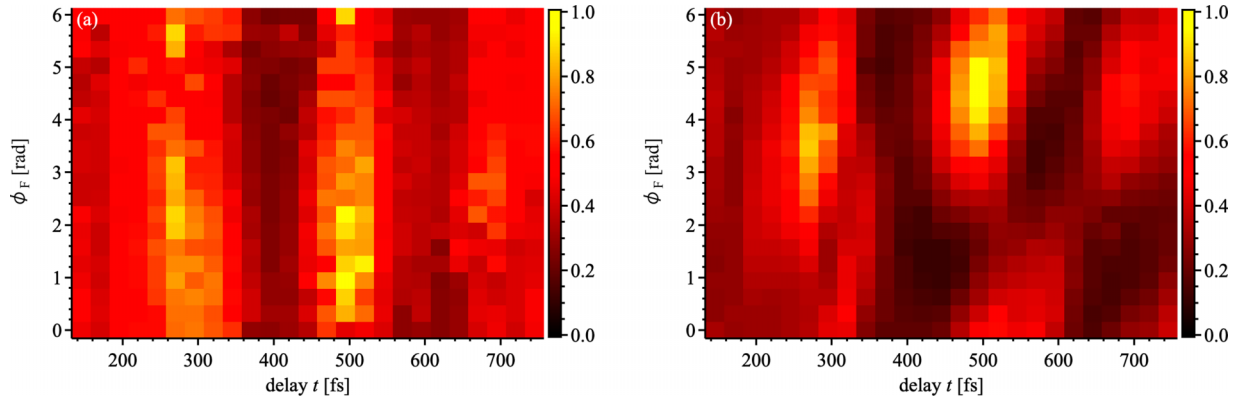


FIG. 5. Normalized photoion map (a) without and (b) with phase jitter correction.

This in turn influences the wave-packet intensities in Fig. 7(b) where all wave packets containing $n = 12$ Rydberg states show a minimum at this value of phase.

The frequencies for excitation of the $n = 11$ and 12 Rydberg states have periods that differ by 0.124 attoseconds, which after 2310 cycles corresponds to 1.7 periods. Similarly, the $n = 12$ and 13 Rydberg states accumulate a phase difference of 1.3 rad after 390 fs. In Fig. 7(b), it can be seen that the maxima of the $n = 11$ and 13 Rydberg state amplitudes are significantly displaced from that of $n = 12$ but not by the estimated phase difference. We assign this discrepancy to the chirp of the pulse; by definition, frequency varies along

the pulse, so that the effective delay will differ for different Rydberg states.

By selecting data with $\phi_F = 4.5$ rad, we observe predominantly the $(11,12)$ and $(12,13)$ wave packets, while other wave packets are excited more weakly. At $\phi_F = 2.6$ rad, the $(11,13)$ wave packet is excited, while others are very weakly excited. Thus we have observed control of the wave packets by means of the phase.

Figure 7(c) shows a map of the wave-packet phase as a function of optical phase. While $|a_n a_m^*|$ and the real and imaginary parts of a_n have a sinusoidal dependence on optical phase, the wave-packet phase is more complicated. In par-

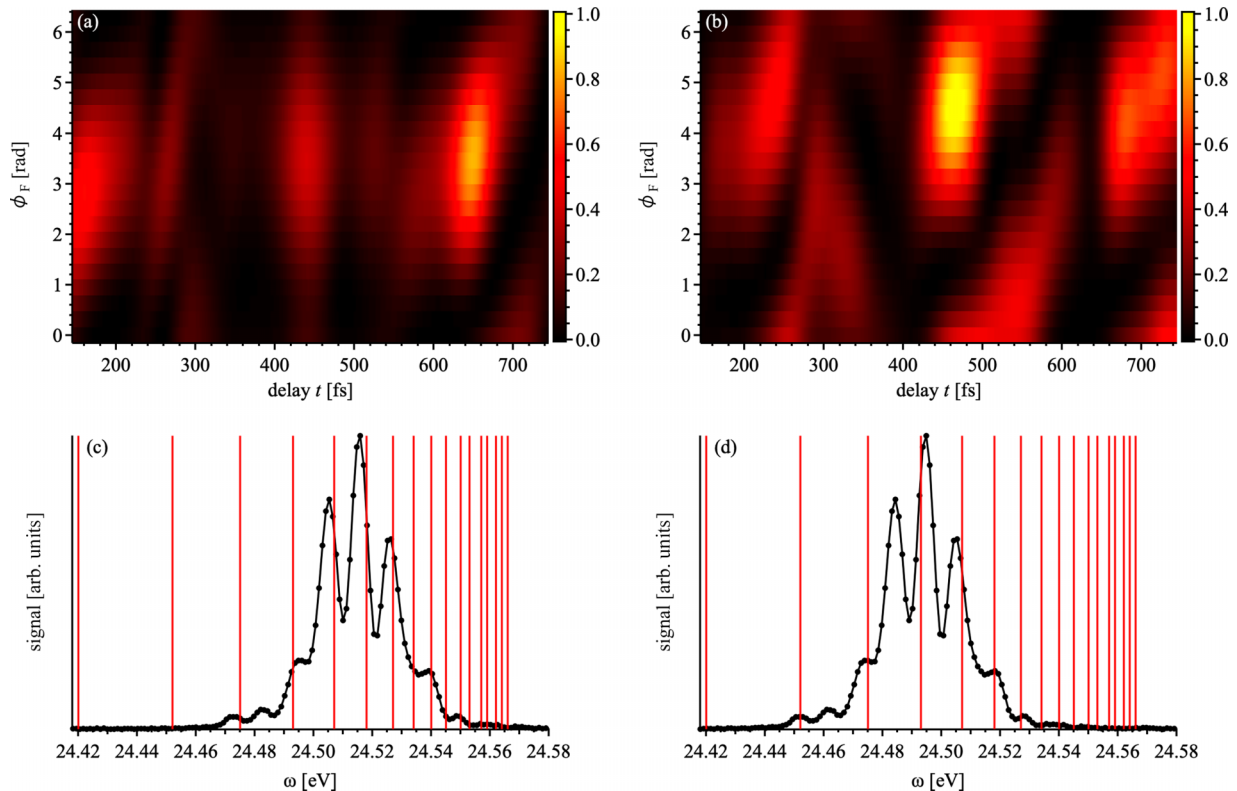


FIG. 6. Photoion map simulation of Dataset 1 ($\tau = 390$ fs) (a) before correction of spectrometer energy offset, $\omega_F = 24.513$ eV, and (b) after correction of spectrometer energy offset, $\omega_F = 24.492$ eV. The absolute normalization is arbitrary but equal for both maps. Panels (c), (d) show the same photon spectrum as Fig. 2 before and after offset correction; red sticks indicate the positions of Rydberg states with $n = 9-25$.

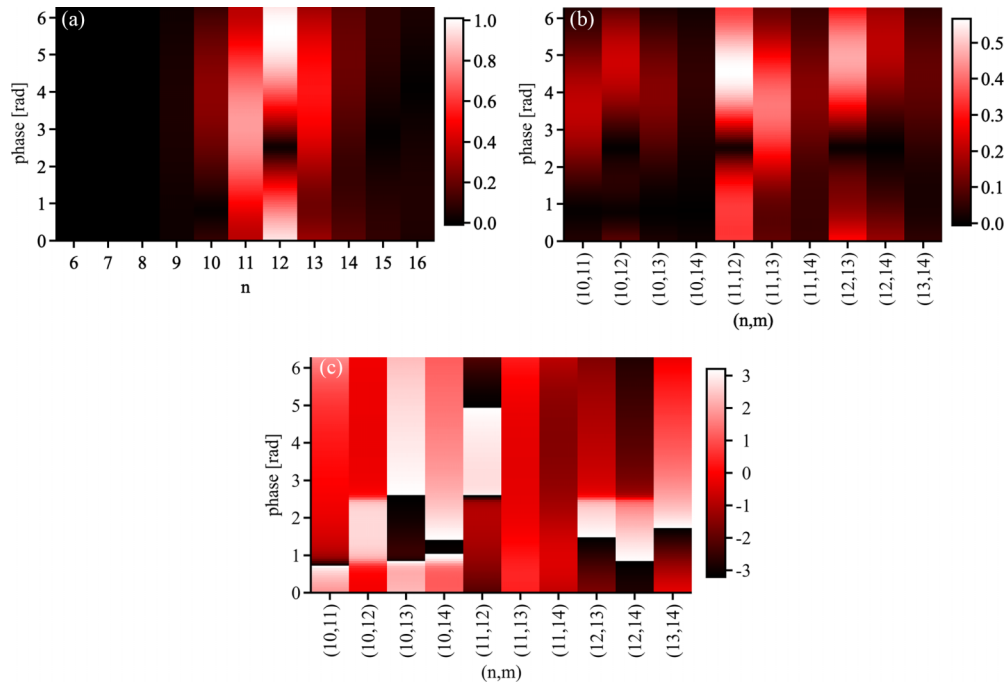


FIG. 7. (a) Relative amplitude $|a_n|$ (normalized to the maximum of $|a_{12}|$) of each quantum state n in the wave packet as a function of optical phase. (b) Relative contribution $|a_n a_m^*|$ (normalized to the maximum of $|a_{12}|^2$) of each wave-packet beating component (n, m) . (c) Wave-packet phase (from $-\pi$ to π) as a function of optical phase. The calculation is performed at an asymptotically large value of t , 900 fs, using the best-fit parameters reported in Table I, except $\omega_F = 24.492$ eV: see the caption of Fig. 6.

ticular, phase jumps occur when the modulus $|a_n a_m^*|$ is zero, and this is apparent in the sudden changes from maximum to minimum phase. The quantity of interest is the relative phase difference between wave packets, and this can be read from Fig. 7(c). For example, the (11,12) wave packet has maximum amplitude at optical phase 4.6 rad, when the wave-packet phase is 3.0 rad. At 4.6 rad, the (11,13) wave packet has a phase of -0.3 rad, so the difference between the wave packets is 3.3 rad at this optical phase setting.

VI. RESULTS AND ANALYSIS OF PARTIALLY OVERLAPPING PULSES

It has been pointed out that in the case of partially overlapping pulses, the envelope of the pulse pair is modulated as a function of the phase of the seed pulse frequency ω_0 and of its multiples up to $\eta\omega_0$ ($\eta =$ the FEL harmonic number of choice), due to interference between the components of the two pulses. This modulation is relatively weak and can be detected using sensitive lock-in techniques [11], but the present signal-to-noise ratio of the photon spectrum is not sufficient to do so, especially in the presence of chirp, drift of the central wavelength during data acquisition, and overbunching. Figure 8(b) shows a calculated map, taking account of lower frequencies than $5\omega_0$, the FEL frequency.

Due to this complication, for Dataset 2 ($\tau = 130$ fs), we used the simpler method of Uhl *et al.* [13] to assign the phase of the overlapping pulses, namely the position of the absolute maximum of the interference fringes. This amounts to ignoring all modulations except that at harmonic $\eta = 5$, i.e., still assuming that the twin pulse is uniquely defined by $\phi_F \in [0, 2\pi]$, whereas it is more precise to consider $\phi_F \in [0, 2\eta\pi]$.

Figure 8(a) shows a map generated from Dataset 2, while Fig. 8(b) shows the map calculated considering five periods of the FEL phase, and the inequivalence of the five periods of the seed is manifest. For instance, in the first period of the FEL radiation, $\phi_F = 0$ to 2π , only weak modulation is visible along the time axis. In the second period, $\phi_F = 2\pi$ to 4π , very strong maxima are visible. For larger values of phase, no interval of 2π is equivalent to any other, and only after five full cycles does the map repeat the structure at $\phi_F = 0$. The calculations used the fit parameters from Dataset 1, Table I, and assume that source parameters for the two datasets differ only in the time delay between the pulses. Figure 8(c) shows the same calculation, with folding of the phase to correspond to a single period of the FEL phase. This folded map shows a reasonably good agreement with the experimental map, with broader features in the experiment which could be due to a number of factors. The dark band of minima at about 4 rad is reproduced well, and the maxima of the oscillations at about 1 rad are in good agreement with the experiment. The total drift is about 20 meV, approximately one bandwidth of the radiation.

The calculated map in Fig. 8(b) clearly shows that modulation effects by phases other than that of the FEL (fifth harmonic of the seed) are present for this case of partially overlapping pulses. The origin of this modulation can be understood qualitatively by considering the simplified case of zero chirp and weak seeding that does not induce overbunching [that is, a small value of the argument of the Bessel function in Eq. (1)]. Then the electric field is described by Eq. (3), with the exponential term set to a value of 1. Equation (A6) in the Appendix shows that the electric field consists of an oscillatory part at the carrier frequency (the

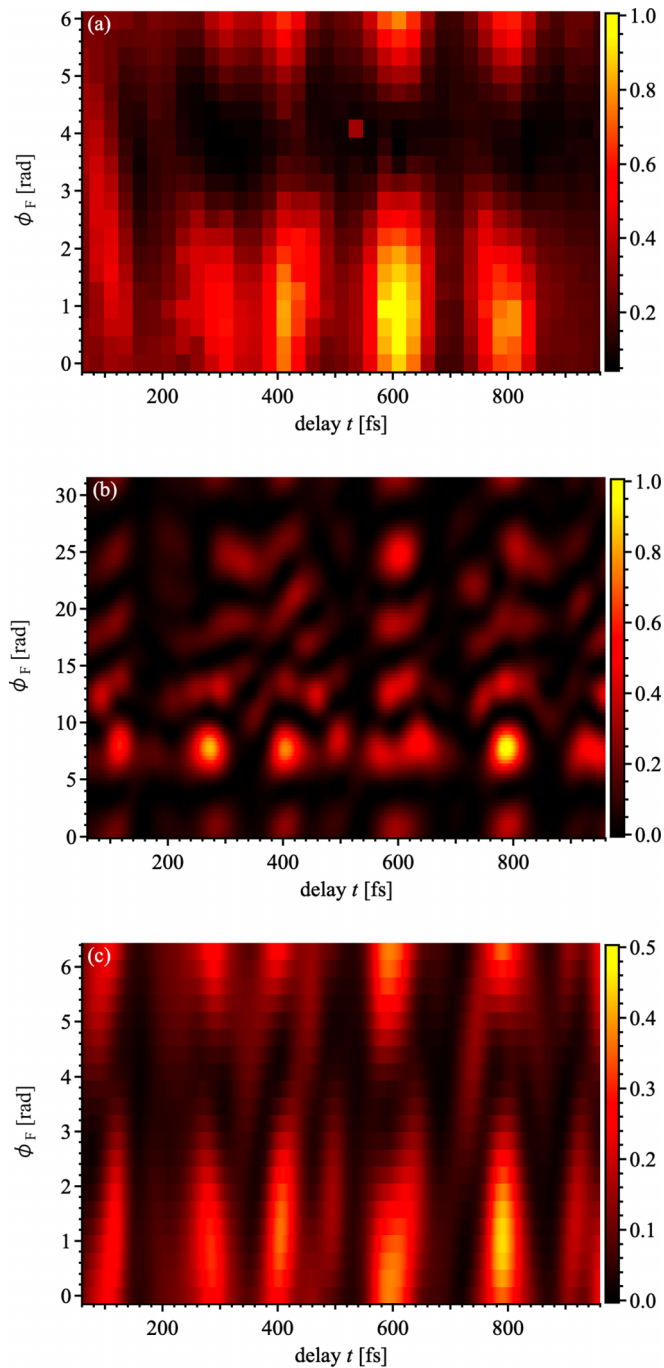


FIG. 8. (a) Delay-phase map for Dataset 2 (130 fs pulse separation), reconstructed by determination of phase via the position of the fringes in the photon spectrum (as in [13]). (b) Simulation for Dataset 2, without phase folding. The phase scale from 0 to 20π in units of FEL frequency phase corresponds to 0 to 2π in units of seed frequency phase. (c) Simulation with phase folding with $\tau = 130$ fs, $\omega_F = 24.476$ eV, and all other parameters as in Table I.

last exponential term), multiplied by an envelope function containing the integral values of the seed laser phase from 0 to 5. In this case, we conclude that the approximations used provide a reasonable fit of the data, but the problem is underdetermined because there is insufficient signal-to-noise for the detection of subharmonic frequencies in the FEL spectrum.

VII. CONCLUSIONS

We have excited He Rydberg state wave packets using pairs of sequential coherent pulses, and positionized them with IR pulses. The optical phase difference drifted as a function of time, so we tagged the phase of each shot by measuring the photon spectrum, and we recovered the phase relationship between the two pulses for each shot. The procedure for recovering the phase took into account the detailed physics of pulse generation, and the effects of strong seeding, electron beam chirp, and seed laser chirp. Using this information, we sorted the data to obtain time-resolved spectra for individual relative phase values. By selecting data at a particular optical phase, we preferentially excited some wave-packet components and suppressed others, that is, we observed how the phase controlled the dynamics, and we determined the relative phases of the components. The model for this analysis is based on perturbation theory, which assumes a low excitation rate, whereas our experimental conditions implied a high excitation probability. Nevertheless, this procedure worked well for separated pulses, although for temporally overlapping pulses additional phase components at harmonics of the seed pulse appear in the spectrum of the electric field. The ion map can be modeled, using reasonable assumptions, and acceptable agreement with the experiment was found. However, in this case the process is experimentally underdetermined, and the detailed electric field of the partially overlapping pulses cannot be derived from the experimental data.

This work aids in the development of suitable methods for performing wave packet and two-dimensional spectroscopy using FELs, where there are different experimental challenges compared to laboratory-based experiments.

The data supporting these results are available from the corresponding authors upon reasonable request.

ACKNOWLEDGMENTS

We thank the staff of the FERMI facility for their technical support and for ensuring the smooth operation of the experiments, and especially Enrico Allaria for fruitful discussions. S.T.P. is supported by the U.S. Department of Energy, Office of Science, Office of Basic Energy Sciences, Division of Chemical Sciences, Geosciences, and Biosciences under Contract No. DE-AC02-06CH11357. D.Y. acknowledges a Grant-in-Aid of Tohoku University Institute for Promoting Graduate Degree Programs Division for Interdisciplinary Advanced Research and Education for support. K.U. acknowledges the Research Program of Dynamic Alliance for Open Innovations Bridging Human, Environment and Materials and IMRAM project for support. H.I. and F.L. acknowledge funding from NSERC and FRQNT. P.E.-J. and J.P. acknowledge the support of the Swedish Research Council (2017-04106) and the Swedish Foundation for Strategic Research (FFL12-0101). J.M., A.O., and E.R.S. would like to acknowledge support from the Swedish Research Council (VR) and the Crafoord Foundation. J.M. and A.O. would like to acknowledge support from the Wallenberg Center for Quantum Technology (WACQT) funded by The Knut and Alice Wallenberg Foundation (KAW 2017.0449). E.R.S. would like to acknowledge

support from the Royal Physiographic Society of Lund. G.S., P.K.M., and M.M. acknowledge funding from the European Union Horizon 2020 research and innovation program under the Marie Skłodowska-Curie Grant Agreement No. 641789 MEDEA. G.S., D.E., and R.S. acknowledge funding from

the Deutsche Forschungsgemeinschaft (DFG) [IRTG CoCo (2079), QUTIF SA 3470/2]. The ELI-ALPS project (GINOP-2.3.6-15-2015-00001) is supported by the European Union and cofinanced by the European Regional Development Fund.

APPENDIX

1. Histogram plots

Figure 9 presents an illustration of the best-fit parameter histograms. Note the larger, and more scattered, values for the chirp and σ_F .

2. Consideration of δ -like pulses

For two δ -like pulses separated by a time $\tau < 0$, Eq. (10) simplifies to

$$a_n(t) = \begin{cases} 0, & t < \tau, \\ -\frac{i\mu}{n^{3/2}} e^{-i\omega_n t} e^{-i\omega_{1n}\tau - i\phi_F}, & \tau \leq t < 0, \\ -\frac{i\mu}{n^{3/2}} e^{-i\omega_n t} (e^{-i\omega_{1n}\tau - i\phi_F} + 1), & t \geq 0, \end{cases} \quad (\text{A1})$$

and the summands in Eq. (14) simplify to

$$w_k w_m (a_k a_m^* + a_k^* a_m) = \begin{cases} \frac{2\mu^2}{k^3 m^3} \cos[\omega_{km}(t - \tau)], & -\frac{\tau}{2} \leq t < \frac{\tau}{2}, \\ \frac{8\mu^2}{k^3 m^3} \cos[\omega_{km}(t - \frac{\tau}{2})] \cos(\frac{\omega_{1k}\tau + \phi_F}{2}) \cos(\frac{\omega_{1m}\tau + \phi_F}{2}), & t \geq \frac{\tau}{2}, \end{cases} \quad (\text{A2})$$

$$= \frac{4\mu^2}{k^3 m^3} \cos\left[\omega_{km}\left(t - \frac{\tau}{2}\right)\right] \left[\cos(\Omega_{km}\tau + \phi_F) + \cos\left(\frac{\omega_{km}\tau}{2}\right) \right] t \geq \frac{\tau}{2}, \quad (\text{A3})$$

where $\Omega_{km} = (\omega_{1k} + \omega_{1m})/2$, and $\omega_{km} = \omega_{1k} - \omega_{1m}$.

Thus, in this approximation, the map can be considered as a sum of constants (for $k = m$) plus cosine functions whose frequencies are those of the Rydberg wave-packet components; their amplitude depends on the delay τ and the phase ϕ_F .

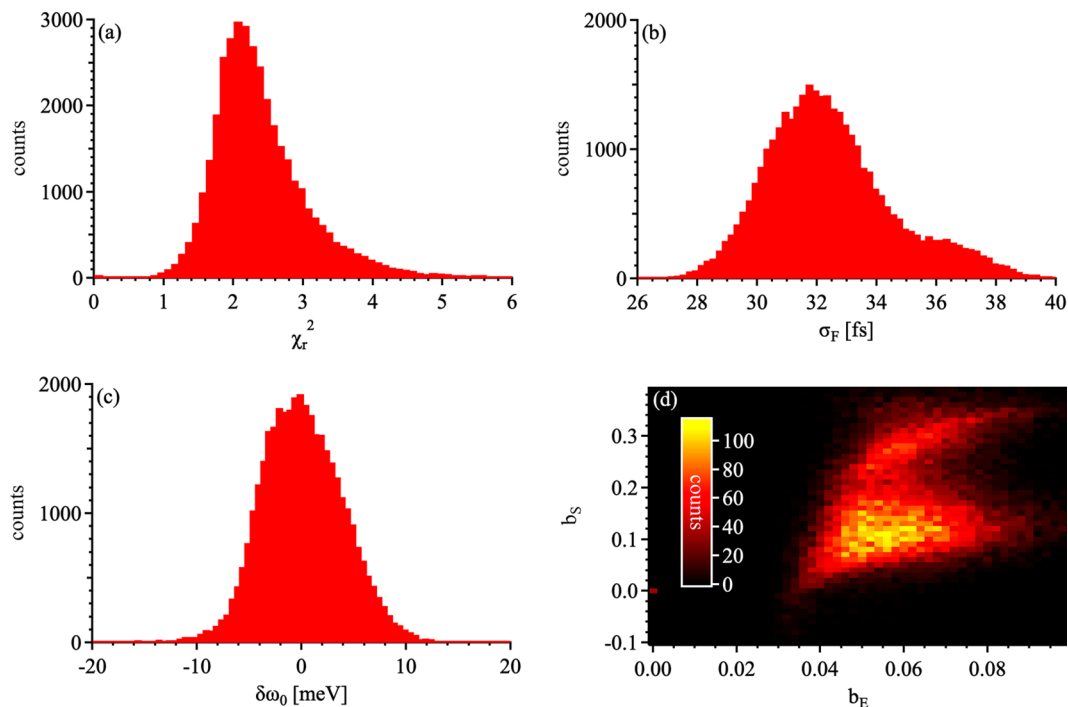


FIG. 9. Best-fit parameter histograms, with dispersion neglected. (a) χ_r^2 , (b) σ_F , (c) $\delta\omega_0$, (d) b_E , b_S . Cf. Fig. 3.

3. Simplified expressions for partially overlapping pulses

For the case of partially overlapping pulses, far from overbunching, and zero chirp, a simplified expression based on Eq. (4) can be written

$$E(t) \propto [A(t)]^\eta \quad (\text{A4})$$

$$A(t) = \exp \left[-\left(\frac{t - \tau/2}{2\sigma} \right)^2 + i\omega_0(t - \tau/2) - i\phi/2 \right] + \exp \left[-\left(\frac{t + \tau/2}{2\sigma} \right)^2 + i\omega_0(t + \tau/2) + i\phi/2 \right]. \quad (\text{A5})$$

This equation has an analytical Fourier transform, which for the present case of $\eta = 5$ can be written

$$\hat{E}(\omega) \propto \sigma e^{i\phi/2} \left\{ e^{i\tau\omega/2} + e^{5i\phi - i\tau\omega/2} + 10e^{-\frac{3\tau^2}{10\sigma^2}} [e^{2i\phi + i\tau/10} + e^{3i\phi - i\tau\omega/10}] + 5e^{-\frac{\tau^2}{5\sigma^2}} [e^{i\phi + 3i\tau\omega/10} + e^{4i\phi - 3i\tau\omega/10}] \right\} \exp \left[-\frac{\sigma^2}{5} (\omega + 5\omega_0)^2 \right]. \quad (\text{A6})$$

This expression consists of the sum of terms containing all integral values of the seed phase ϕ from 0 to 5, all of which are multiplied by the last exponential term. This exponential can be regarded as describing the carrier frequency $5\omega_0$, with a Gaussian profile, and whose width is proportional to $1/\sigma$. The first sum (in curly brackets) can be regarded as an envelope function. Note that for nonoverlapping pulses, i.e., $\tau \gg \sigma$, all terms in the sum vanish except for the first two, and we recover the expression in Eq. (5) (with chirp set to zero).

-
- [1] D. J. Tannor, R. Kosloff, and S. A. Rice, Coherent pulse sequence induced control of selectivity of reactions: exact quantum mechanical calculations, *J. Phys. Chem.* **85**, 5805 (1986).
- [2] R. Kosloff, S. A. Rice, P. Gaspard, S. Tersigni, and D. J. Tannor, Wavepacket dancing: Achieving chemical sensitivity by shaping light pulses, *Chem. Phys.* **139**, 201 (1989).
- [3] S. A. Rice, New ideas for guiding the evolution of a quantum system, *Science* **258**, 412 (1992).
- [4] L. D. Noordam, D. I. Duncan, and T. F. Gallagher, Ramsey fringes in atomic Rydberg wave packets, *Phys. Rev. A* **45**, 4734 (1992).
- [5] M. Berholts, R. Knut, R. Stefanuik, H. Wikmark, S. Saha, and J. Söderström, Quantum watch and its intrinsic proof of accuracy, *Phys. Rev. Res.* **4**, 043041 (2022).
- [6] K. Ohmori, H. Katsuki, H. Chiba, M. Honda, Y. Hagihara, K. Fujiwara, Y. Sato, and K. Ueda, Real-time observation of phase-controlled molecular wave-packet interference, *Phys. Rev. Lett.* **96**, 093002 (2006).
- [7] K. Ohmori, Wave-packet and coherent control dynamics, *Annu. Rev. Phys. Chem.* **60**, 487 (2009).
- [8] L.-M. Koll, L. Maikowski, L. Drescher, T. Witting, and M. J. J. Vrakking, Experimental control of quantum-mechanical entanglement in an attosecond pump-probe experiment, *Phys. Rev. Lett.* **128**, 043201 (2022).
- [9] D. Gauthier, P. R. Ribič, G. De Ninno, E. Allaria, P. Cinquegrana, M. B. Danailov, A. Demidovich, E. Ferrari, and L. Giannessi, Generation of phase-locked pulses from a seeded free-electron laser, *Phys. Rev. Lett.* **116**, 024801 (2016).
- [10] A. Wituschek, L. Bruder, E. Allaria, U. Bangert, M. Binz, C. Callegari, G. Cerullo, P. Cinquegrana, L. Gianessi, M. Danailov, A. Demidovich, M. Di Fraia, M. Drabbels, R. Feifel, T. Laarmann, R. Michiels, N. S. Mirian, M. Mudrich, I. Nikolov, F. H. O'Shea *et al.*, Tracking attosecond electronic coherences using phase-manipulated extreme ultraviolet pulses, *Nat. Commun.* **11**, 883 (2020).
- [11] A. Wituschek, L. Bruder, E. Allaria, U. Bangert, M. Binz, C. Callegari, P. Cinquegrana, M. Danailov, A. Demidovich, M. D. Fraia, R. Feifel, T. Laarmann, R. Michiels, M. Mudrich, I. Nikolov, P. Piseri, O. Plekan, K. C. Prince, A. Przystawik, P. R. Ribič *et al.*, High-gain harmonic generation with temporally overlapping seed pulses and application to ultrafast spectroscopy, *Opt. Express* **28**, 29976 (2020).
- [12] D. Uhl, A. Wituschek, R. Michiels, F. Trinter, T. Jahnke, E. Allaria, C. Callegari, M. Danailov, M. D. Fraia, O. Plekan, U. Bangert, K. Dulitz, F. Landmesser, M. Michelbach, A. Simoncig, M. Manfredda, S. Spampinati, G. Penco, R. J. Squibb, R. Feifel *et al.*, Extreme ultraviolet wave packet interferometry of the autoionizing HeNe dimer, *J. Phys. Chem. Lett.* **13**, 8470 (2022).
- [13] D. Uhl, A. Wituschek, U. Bangert, M. Binz, C. Callegari, M. D. Fraia, O. Plekan, K. C. Prince, G. Cerullo, L. Giannessi, M. Danailov, G. Sansone, T. Laarmann, R. Michiels, M. Mudrich, P. Piseri, R. J. Squibb, R. Feifel, S. Stranges, F. Stienkemeier *et al.*, Improved stabilization scheme for extreme ultraviolet quantum interference experiments, *J. Phys. B* **55**, 074002 (2022).
- [14] S. Usenko, A. Przystawik, M. A. Jakob, L. L. Lazzarino, G. Brenner, S. Toleikis, C. Haunhorst, D. Kip, and T. Laarmann, Attosecond interferometry with self-amplified spontaneous emission of a free-electron laser, *Nat. Commun.* **8**, 15626 (2017).
- [15] S. Usenko, D. Schwickert, A. Przystawik, K. Baev, I. Baev, M. Braune, L. Bocklage, M. K. Czwalinna, S. Deinert, S. Düsterer, A. Hans, G. Hartmann, C. Haunhorst, M. Kuhlmann, S. Palutke, R. Röhlberger, J. Rönsch-Schulenburg, P. Schmidt,

- S. Skruszewicz, S. Toleikis *et al.*, Auger electron wave packet interferometry on extreme timescales with coherent soft x-rays, *J. Phys. B* **53**, 244008 (2020).
- [16] D. Schwickert, M. Ruberti, P. Kolorenč, S. Usenko, A. Przystawik, K. Baev, I. Baev, M. Braune, L. Bocklage, M. K. Czwalinna, S. Deinert, S. Düsterer, A. Hans, G. Hartmann, C. Haunhorst, M. Kuhlmann, S. Palutke, R. Röhlberger, J. Rönsch-Schulenburg, P. Schmidt *et al.*, Electronic quantum coherence in glycine molecules probed with ultrashort x-ray pulses in real time, *Sci. Adv.* **8**, eabn6848 (2022).
- [17] Y. Hikosaka, T. Kaneyasu, M. Fujimoto, H. Iwayama, and M. Katoh, Coherent control in the extreme ultraviolet and attosecond regime by synchrotron radiation, *Nat. Commun.* **10**, 4988 (2019).
- [18] T. Kaneyasu, Y. Hikosaka, M. Fujimoto, H. Iwayama, and M. Katoh, Electron wave packet interference in atomic inner-shell excitation, *Phys. Rev. Lett.* **126**, 113202 (2021).
- [19] T. Fuji, T. Kaneyasu, M. Fujimoto, Y. Okano, E. Salehi, M. Hosaka, Y. Takashima, A. Mano, Y. Hikosaka, S.-i. Wada, and M. Katoh, Spectral phase interferometry for direct electric-field reconstruction of synchrotron radiation, *Optica* **10**, 302 (2023).
- [20] K. C. Prince and B. Diviacco, On “Coherent control in the extreme ultraviolet and attosecond regime by synchrotron radiation” by Hikosaka *et al.*, *Nat. Commun.* **10**, 4988 (2019), *Nat. Commun.* **12**, 3784 (2021).
- [21] Y. Hikosaka, T. Kaneyasu, M. Fujimoto, H. Iwayama, and M. Katoh, Reply to “Comment on ‘Coherent control in the extreme ultraviolet and attosecond regime by synchrotron radiation’” *Nat. Commun.* **12**, 3782 (2021).
- [22] V. Lyamayev, Y. Ovcharenko, R. Katzy, M. Devetta, L. Bruder, A. LaForge, M. Mudrich, U. Person, F. Stienkemeier, M. Krikunova, T. Möller, P. Piseri, L. Avaldi, M. Coreno, P. O’Keeffe, P. Bolognesi, M. Alagia, A. Kivimäki, M. D. Fraia, N. B. Brauer *et al.*, A modular end-station for atomic, molecular, and cluster science at the low density matter beamline of FERMI@Elettra, *J. Phys. B* **46**, 164007 (2013).
- [23] B. Ardini, F. Richter, L. Uboldi, P. Cinquegrana, M. Danailov, A. Demidovich, S. D. Ganeshamandiram, S. Hartweg, G. Kurdi, F. Landmesser, M. Michelbach, A. Ngai, I. Nikolov, N. Rendler, F. Stienkemeier, D. Uhl, L. Bruder, G. Cerullo, and C. Manzoni, Generation of interferometrically stable pulse pairs from a free-electron laser using a birefringent interferometer, *J. Phys. B: At. Mol. Opt. Phys.* **57**, 075402 (2024).
- [24] D. Gauthier, P. R. Ribič, G. De Ninno, E. Allaria, P. Cinquegrana, M. B. Danailov, A. Demidovich, E. Ferrari, L. Giannessi, B. Mahieu, and G. Penco, Spectrotemporal shaping of seeded free-electron laser pulses, *Phys. Rev. Lett.* **115**, 114801 (2015).
- [25] J. Gallas, G. Leuchs, H. Walther, and H. Figger, Rydberg atoms: High-resolution spectroscopy and radiation interaction—Rydberg molecules, in *Advances in Atomic and Molecular Physics*, edited by D. Bates and B. Bates (Elsevier, Amsterdam, 1985), Vol. 25, pp. 413–466.
- [26] D. H. Menzel, C. L. Pekeris, and H. Shapley, Absorption coefficients and hydrogen line intensities, *Mon. Not. R. Astron. Soc.* **96**, 77 (1935).
- [27] R. R. Jones, C. S. Raman, D. W. Schumacher, and P. H. Bucksbaum, Ramsey interference in strongly driven Rydberg systems, *Phys. Rev. Lett.* **71**, 2575 (1993).